WSR-88D Sidelobe Contamination: From a Conceptual Model to Diagnostic Strategies for Improving NWS Warning Performance

JAMI B. BOETTCHER[a,b] AND EVAN S. BENTLEY[c]

[a] *Cooperative Institute for Severe and High-Impact Weather Research and Operations, University of Oklahoma, Norman, Oklahoma*
[b] *NOAA/OAR/National Severe Storms Laboratory, Norman, Oklahoma*
[c] *NOAA/NWS/NCEP/Storm Prediction Center, Norman, Oklahoma*

(Manuscript received 21 September 2021, in final form 3 March 2022)

ABSTRACT: Providing timely warnings for severe and potentially tornadic convection is a critical component of the NWS mission, and owing to the associated large reflectivity gradients, sidelobe contamination is possible. This paper focuses on elevation sidelobe contamination appearing in the low-level inflow region of supercells. A qualitative conceptual model of the Weather Surveillance Radar-1988 Doppler (WSR-88D) antenna pattern interacting with supercells is introduced, along with Doppler power spectrum representations of the potential mix of returned power from the main lobe and the sidelobes. These tools inform the multiple ways elevation sidelobe contamination appears in the low levels, primarily below 3 km (10 kft) of radar data. The most common manifestation is somewhat noisy data similar to particulates or biota in clear air. Trained NWS forecasters are accustomed to mentally filtering out noisy clear-air returns as less important. Elevation sidelobe contamination can be mixed with the three-body scatter spike (TBSS) artifact, though the TBSS remains the more salient feature. The most consequential form is the apparent circulation, and when it is incorrectly interpreted as valid, contributes to the false alarm ratio (FAR) for NWS tornado warnings. Quantitative results on the effect of elevation sidelobe contamination on FAR are presented. Diagnostic techniques are emphasized, and with familiarization, can be used in real-time warning operations to identify the apparent circulation as either valid or an imposter. Identification of these contaminated velocity signatures offers a unique opportunity to reduce the NWS tornado warning FAR without also reducing the probability of detection (POD).

SIGNIFICANCE STATEMENT: The WSR-88D weather radars provide overall high-quality data for users. However, with some severe thunderstorms, an artifact called elevation sidelobe contamination can produce what looks like a rotation signature, but it may not be real. These ambiguous velocity signatures can contribute to tornado warnings based on rotation signatures that are false circulations. This paper specifically focuses on elevation sidelobe contamination due to its impact on tornado warning decisions. Diagnostic techniques, including several examples, are presented here to aid the reader in correctly identifying elevation sidelobe contamination and why it may occur. Correct identification of an apparent circulation as an imposter due to contamination is a unique opportunity to improve NWS tornado warning performance by reducing warning false alarms.

KEYWORDS: Data quality control; Radars/Radar observations; Operational forecasting; Decision making

1. Introduction

Radar base data analysis is foundational to the NWS severe convection warning domain (Andra et al. 2002; Brotzge and Donner 2013). The deployment of the WSR-88D network has led to significant progress in understanding severe storm behavior and feature identification. Additional WSR-88D upgrades such as superresolution radar data in 2007 (Brown et al. 2002, 2005a; Torres and Curtis 2007), dual-polarization data in 2012 (Saxion and Ice 2012), and SAILS/MESO-SAILS in 2014 (Chrisman 2011, 2014) have furthered the ability to more closely examine severe convective storms. However, warning performance, when measured as probability of detection (POD) and false alarm ratio (FAR), has remained approximately constant since 2011 (Brooks and Correia 2018). In fact, POD has been dropping. This was speculated by Brooks and Correia (2018) to be attributed to shorter default duration warnings and an apparent emphasis on reducing false alarms. This POD reduction is expected if FAR reduction is desired given the correlation of FAR and POD. Typically, greater POD is preferred versus lower FAR due to the asymmetric penalty function (Brooks 2004). However, Bentley et al. (2021) suggests that a reduction in FAR can be accomplished with minimal reduction in POD when certain conditions are present. One of these conditions was correct identification of contaminated velocity data, of which an estimated 90% was due to sidelobe contamination.

This paper provides both a conceptual model and diagnosis techniques with the goal of improving real-time identification of sidelobe contamination. Though outside the scope of this study, for all the supercell cases presented in this paper, the authors recognize the importance of the mesoscale environment and its role in warning decision-making. Awareness of the mesoscale environment is an important component to assess tornadic potential even when the low-level velocity signature may be contaminated. If the environment is favorable for tornadoes, a tornado warning may be justified even if sidelobe contamination is impacting low-level velocity data. Diagnostic tools provided in

Corresponding author: Jami B. Boettcher, jami.b.boettcher@noaa.gov

DOI: 10.1175/WAF-D-21-0155.1

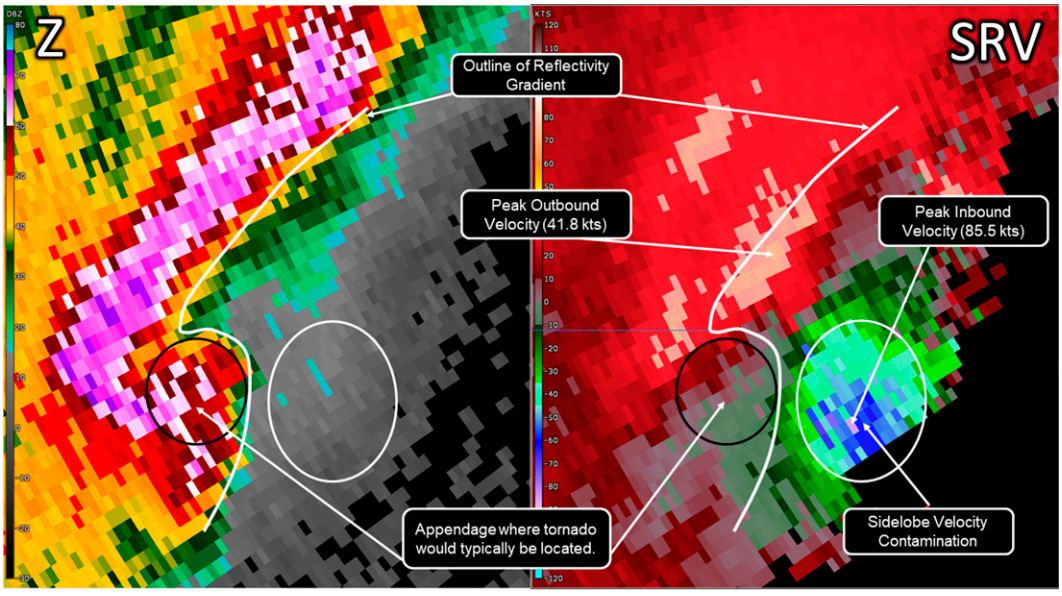

FIG. 1. Image adapted from Bentley et al. (2021) showing a case of ESLC mimicking a strong low-level circulation from the WSR-88D radar.

this paper support real-time identification of sidelobe contamination that presents as an apparent circulation with the potential for improved NWS tornado warning performance through a reduction in the FAR.

An extensive literature review showed that Piltz and Burgess (2009) was the only operationally relevant literature on the topic of sidelobe contamination and its impact on warning operations. Later, Nai et al. (2020) introduced the term elevation sidelobe contamination (hereafter abbreviated as ESLC) for what is typically referred to as vertical sidelobe contamination. Another discovery from the study conducted by Nai et al. (2020) is that ESLC more often presents as noisy velocity (V) data collocated with high spectrum width (SW) and low correlation coefficient (CC) in a supercell's low-level inflow region. This paper bridges the latest data-based understanding of sidelobe contamination with its impacts on warning decisions to provide a comprehensive guide for operational WSR-88D users to better understand and recognize sidelobe contamination. Specifically, it underscores the relevance of ESLC, given the unique nature in which WSR-88D sidelobes can yield bogus circulations owing to the intense vertical reflectivity gradients often present in supercell thunderstorms.

Figure 1, adapted from Bentley et al. (2021), provides an example of a critical subset of ESLC, which presents as an apparent circulation, increasing the challenge of real-time diagnosis of tornado potential. When a storm is well sampled (i.e., the lowest beam is below approximately 1.2 km or 4 kft) and has an obvious "hook echo," the tornadic circulation is almost always located within this hook echo. In the absence of a hook, valid circulations are nearly always associated with sufficient reflectivity for precipitation (i.e., typically >20 dBZ), though there are rare exceptions (Bluestein et al. 2007). Circulations or portions of circulations that appear in low-returned-power regions, such as the low-level inflow, are suspicious.

An apparent circulation is defined by a velocity signature with adjacent inbound/outbound velocities, which, at first glance, appears to indicate rotation. However, one of the clues of the circulation's validity can be the lack of characteristics associated with a typical tornadic signature in storm-relative velocity (SRV). A typical tornadic signature has a mostly uniform increase in SRV as one approaches the center of circulation. This speed gradient is a distinctive textural structure, as depicted in Fig. 2. Also, when comparing the SRV peak magnitudes within the inbound and outbound components, they are typically not significantly greater on one side of the circulation than the other. The more accurate the storm motion used to generate SRV, the more "balanced" the respective speed maxima values. These characteristics of valid circulations, and the use of maxima for both inbound and outbound components, are applied to apparent circulations in this paper in order to distinguish and identify those who are imposters.

We examined a subset of the tornado-warned supercells with V contamination from the Bentley et al. (2021) dataset to investigate the complex ways that ESLC contributes to spurious WSR-88D data and the resultant impacts on base data analysis. Though ESLC is also possible with quasi-linear convective systems (QLCS), the much shorter time duration of ESLC compared to supercells makes real-time recognition much more difficult. With QLCS, features such as reflectivity cores aloft and echo overhang are typically not persistent in the same way as with supercells. By providing the structure for ESLC over longer time durations, supercells better reveal the complex ways this contamination manifests in the data.

This examination was done using the Gibson Ridge level-II (GR-2) Analyst radar-viewing software (http://grlevelx.com/gr2analyst_2/) to view archived WSR-88D level-II single site radar data from the NEXRAD archive hosted by Amazon

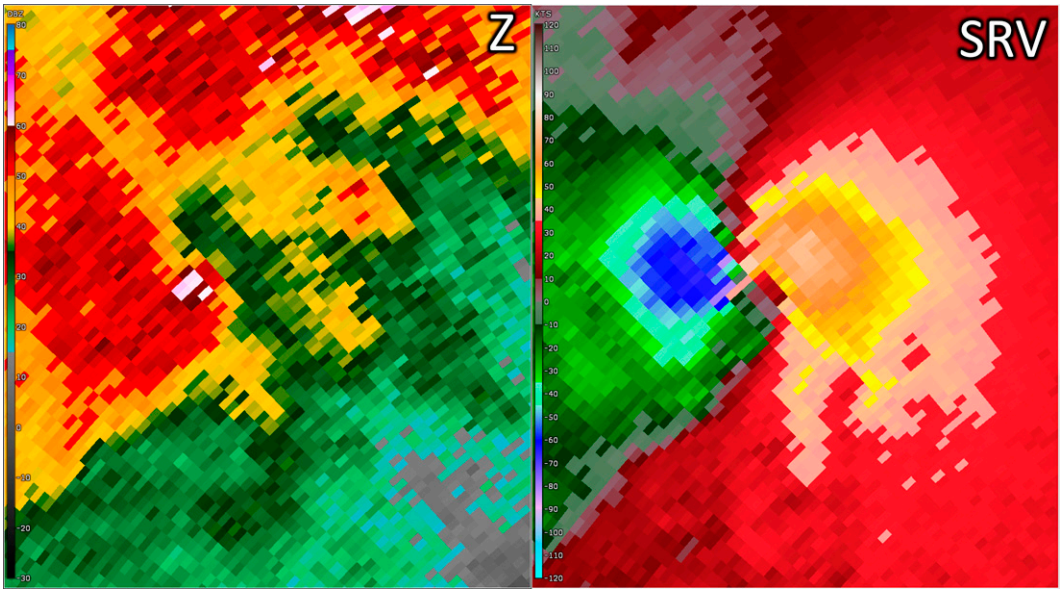

FIG. 2. Example of (left) a tornadic circulation with reflectivity (Z) and (right) storm-relative velocity (SRV). The inbound and outbound components are relatively balanced in size compared to one another, as well as the maxima.

web Services. Radar images in this paper were captured from GR-2 Analyst, and the displays use units such as kilofeet (kft) and nautical miles (n mi), which are commonly used in operational meteorology. Along with reflectivity (Z), SRV, and SW, the dual-polarization variable CC was the most useful for ESLC identification. CC conveys crucial information about the hydrometeor type (e.g., rain, hail) and consistency within the body of the supercell, while within ESLC, CC is usually noisy and suggests nonprecipitation. There are exceptions where the ESLC CC values are still noisy but suggestive of hail. This could occur for supercells with extensive hail within the updraft and overhang encountered by the sidelobes such that the returned power is so dominant, the diversity of scatterers encountered by the sidelobes is suggestive of hail in CC, and some of these exceptions are presented herein.

This paper offers one of the tools developed from the survey of supercells: a qualitative conceptual model of the WSR-88D antenna pattern as it relates to the placement of the main lobe and sidelobes within the structure of a supercell. Using graphics of the Doppler power spectrum, we illustrate the possible mixes of returned power from the main lobe compared to the sidelobes to enhance our understanding of how sidelobe contamination presents in the WSR-88D base data. In this work, base data refers to the images (Z, SRV, SW, and CC) generated directly from the returned signal. In an effort to improve NWS tornado warning performance, the authors developed and refined tools, applicable in real-time warning operations, for diagnosing an apparent circulation as an imposter, or invalid circulation. The conceptual model and diagnostic tools are intended to support NWS warning decision-making, and to inform all users of WSR-88D data.

2. A qualitative look at WSR-88D antenna pattern interactions with large reflectivity gradients

We begin with the fundamentals for the occurrence of WSR-88D sidelobe contamination from a qualitative perspective. The first is a visualization of the WSR-88D antenna radiation pattern geometry in azimuth and elevation, with a focus on the main lobe and multiple sidelobes. The second is the type of weather event that presents Z gradients large enough that, while the main lobe is sampling generally weakly reflective scatterers, the sidelobes are sampling highly reflective scatterers over a volume of space surrounding the main lobe. This phenomenon is generally rare, but it typically occurs within one of the most challenging domains for NWS warning forecasters: severe, and potentially tornadic, convection. The use of Z in this paper describes either the radar reflectivity product, or the underlying (i.e., not seen on the products) linear reflectivity values. The use of dBZ refers to the logarithmic radar reflectivity factor units of the Z products.

Our qualitative visualization of antenna sidelobe contamination begins with the WSR-88D antenna radiation pattern, which covers a three-dimensional volume in space. The WSR-88Ds were designed and built based on clearly defined specifications for high performance (NOAA 1991), and their respective antenna patterns can be expected to be very similar. For reference, there is one WSR-88D whose antenna pattern has been directly measured, the National Severe Storms Laboratory research WSR-88D, the KOUN radar in Norman, Oklahoma. Figure 3a depicts a two-dimensional cross section of KOUN's antenna radiation pattern with the main lobe centered at 0° and sidelobes extending to just beyond ±12.5° in azimuth. To discern the relative peak powers of the sidelobes, it is common to display antenna patterns normalized relative to the peak power. The sidelobes extend ±180° away from the main lobe, with

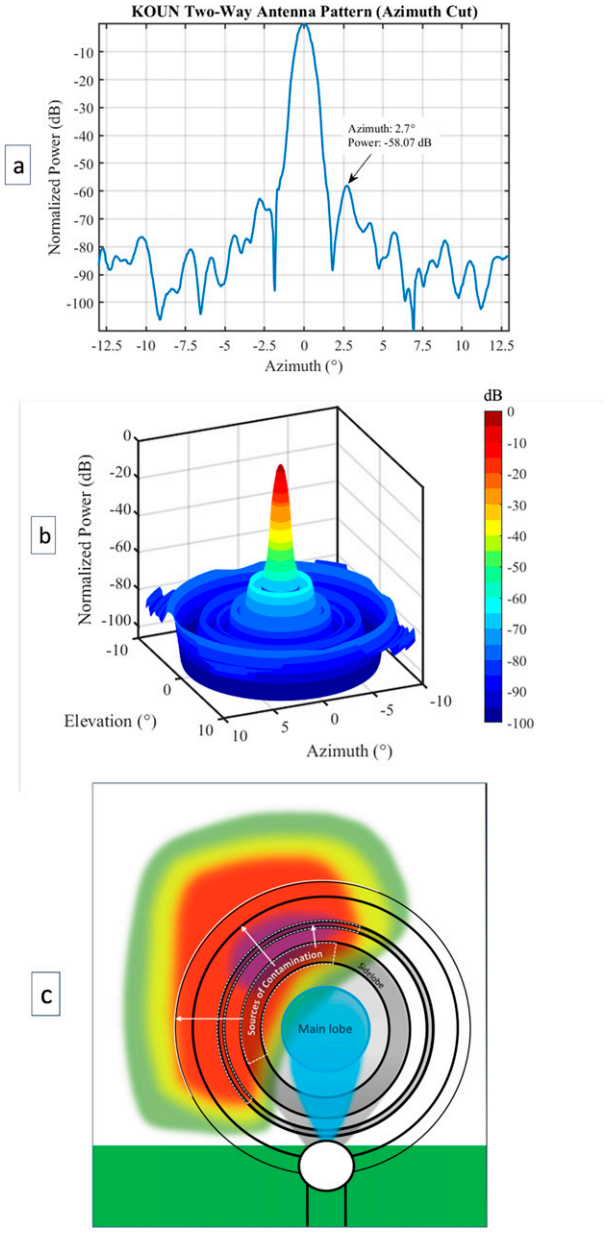

FIG. 3. (a) Measured KOUN WSR-88D antenna radiation pattern in blue, with the main lobe centered at 0° azimuth and the first sidelobe position and power level relative to the main lobe noted. (b) KOUN measured antenna radiation pattern rotated about the main lobe centerline. (c) The perspective of the radar antenna pattern and its projection upon a vertical cross section of a supercell. The main lobe is striking the low-level inflow storm region, while multiple sidelobes strike the supercell's overhang.

magnitude becoming lower with increasing azimuthal distance away from the main lobe. Note the first sidelobe at 2.7° off the main lobe has −58.07 dB two-way transmitted power compared to that of the main lobe. This means that in the absence of large Z gradients, the returned power from the first sidelobe will be $\sim 10^{-6}$ (linear units) smaller than the returned power from the main lobe.

There is always some returned power from all the sidelobes, which exist in azimuth away from the main lobe. In the absence of large Z gradients (generally >55 dBZ within ~3° of azimuth or elevation for the first sidelobe), the main lobe returned power completely dominates that from the sidelobes. In the presence of large Z gradients, accumulated returned power from multiple sidelobes can be sufficient to nearly equal or even dominate the returned power from the main lobe. Thus, an emphasis on the first sidelobe level in Fig. 3a is not sufficient to understand our proposed conceptual model of the mechanism for WSR-88D sidelobe contamination. The cumulative returned power from all the sidelobes can return enough power to result in sidelobe contamination, in multiple forms, and occurs more frequently than the authors initially expected.

Figure 3b is a simplified illustration of the KOUN antenna pattern as a three-dimensional volume, generated by taking the cross section from Fig. 3a and rotating it about the main lobe centerline. This technique has the limitation of presenting the volumetric antenna pattern as perfectly axisymmetric about the main lobe centerline, though there is some variation. From Doviak (2017), ignoring the sidelobe ridges from the struts, the measured WSR-88D antenna pattern demonstrates nearly circular symmetry about the main lobe centerline. The approximation in Fig. 3b is sufficient for our purpose, which is to visualize that sidelobes surround the main lobe in all directions. Sidelobes also extend away from the main lobe beyond the ±10° bounds in Fig. 3b. The cumulative returned power from sidelobes extending well beyond the main lobe supports our qualitative understanding of ESLC, previously identified as "vertical" sidelobe contamination (Piltz and Burgess 2009). The schematic in Fig. 3c further demonstrates the projection of the radar antenna pattern upon the supercell structure. The main lobe is striking the low-level inflow region, while multiple sidelobes that encircle the main lobe are striking the supercell overhang.

The essential weather-related ingredient for sidelobe contamination to occur is a large Z gradient, which is typically present with severe convection. For example, an intense hail core (Fig. 4) can exhibit a gradient from near 70 dBZ to near 20 dBZ within just a few degrees in azimuth. When the main lobe is sampling the clear air adjacent to this storm core (radar located south of the storm, indicated by the arrow and suggested beam spreading icon in Fig. 4), the sidelobes are returning sufficient power, compared to the main lobe, that weak values (<20 dBZ) are assigned to the clear air (blue arrow). In this example, the contamination extends about 15° in azimuth away from the storm core. Even when the main lobe is sampling clear air well away from the storm core, multiple sidelobes are sampling the core and returning sufficient power to generate contamination. This type of WSR-88D sidelobe contamination is referred to as azimuthal sidelobe contamination, due to the azimuthal direction of the contaminated echoes. Though it can occur at varying radar elevation angles, this type of sidelobe contamination is rarely an operational concern. The source of the contamination, the gradient that produces it, is apparent on the same radar image in dBZ units, thus it is straightforward to identify as sidelobe contamination in real time. Azimuthal sidelobe contamination is also often accompanied by a three-body scatter spike (TBSS; Lemon 1998) due to the radar-viewing angle (gray arrow). The TBSS is down

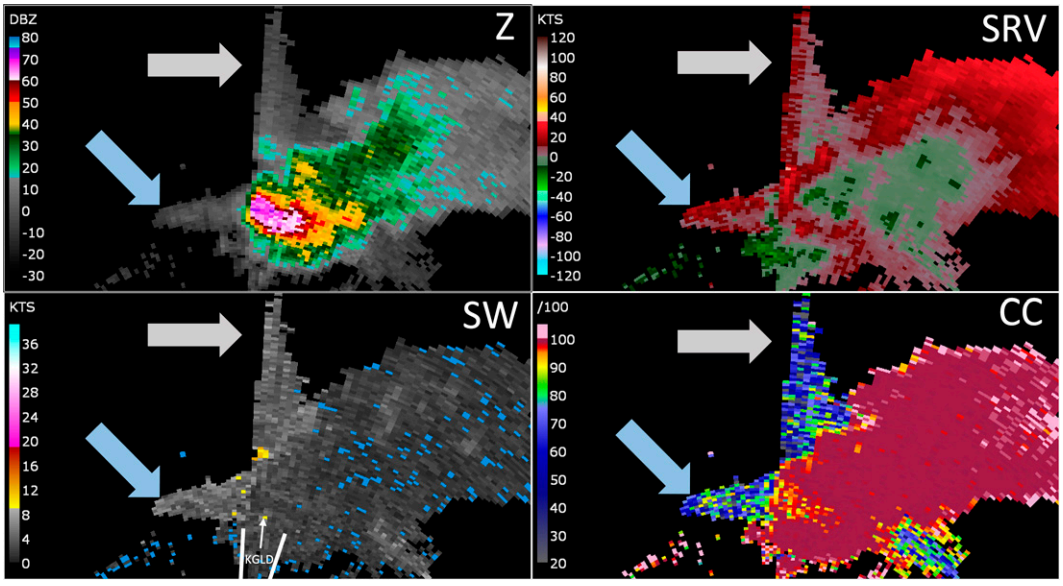

FIG. 4. Radar data from Goodland, KS (KGLD), 2202 UTC 30 Jul 2013 at 12.5°, (top left) Z, (top right) SRV, (bottom left) SW, and (bottom right) CC. The radar location and viewing angle is shown in the bottom-left panel. The azimuthal sidelobe contamination is indicated by the blue arrow and the TBSS by the gray arrow.

radial from the storm core, while azimuthal sidelobe contamination is perpendicular to the TBSS (radial) direction, and both increase confidence in the presence of large hail. The remainder of this paper addresses ESLC, which is more difficult to diagnose in real time, and the resultant impacts on NWS tornado warning performance.

Some storms, particularly supercells, produce Z gradients that exist vertically and at angles up to 90° from the vertical plane. A specific user-defined cross section technique to visualize this important concept is presented in Fig. 5. Figure 5a depicts Z at the 0.5° elevation angle of a supercell sampled by the Boston, Massachusetts (KBOX), radar on 4 August 2015, with the white line indicating the basis for a user-defined cross section, drawn from left to right (labeled from x to y) from the perspective of the radar-viewing angle. The goal is to view this storm from the perspective of the antenna pattern by generating a cross section normal to the radar beam orientation, with the main lobe sampling the low-level clear-air inflow region at 0.5° while the multiple sidelobes are sampling the storm's overhang aloft. The dBZ data depicted in Fig. 5a and in multiple images in this paper are range normalized fields derived from the returned signal power. The planar cross-section analyses are performed at an approximately fixed range from the radar, perpendicular to the radar beam orientation at 0.5°, such that any range normalization differences are negligible. This allows us to use a Z cross section as a qualitative representation of the sources (main lobe and sidelobes) of the returned power for the Z and power weighted SRV and SW radar products.

The resultant cross section cut from left to right normal to the radar beam orientation is presented in Fig. 5b. The maximum height for this and all the cross sections in this paper is displayed as 60 kft, or 18 km. As the main lobe is sampling

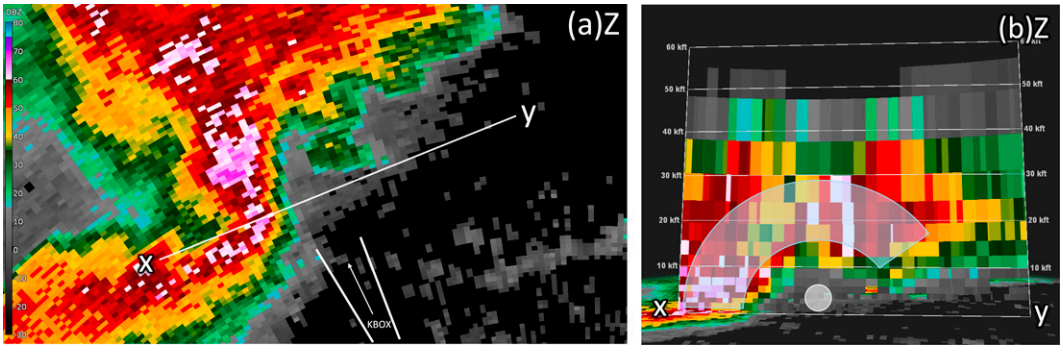

FIG. 5. Radar data from KBOX 1949 UTC 4 Aug 2015 with (a) 0.5° Z with the white line indicating orientation of a user-defined cross section along the white line left to right normal to the outgoing radar beam and (b) Z cross section with the shaded arc revealing the extent of highly reflective hydrometeors aloft that the sidelobes encounter.

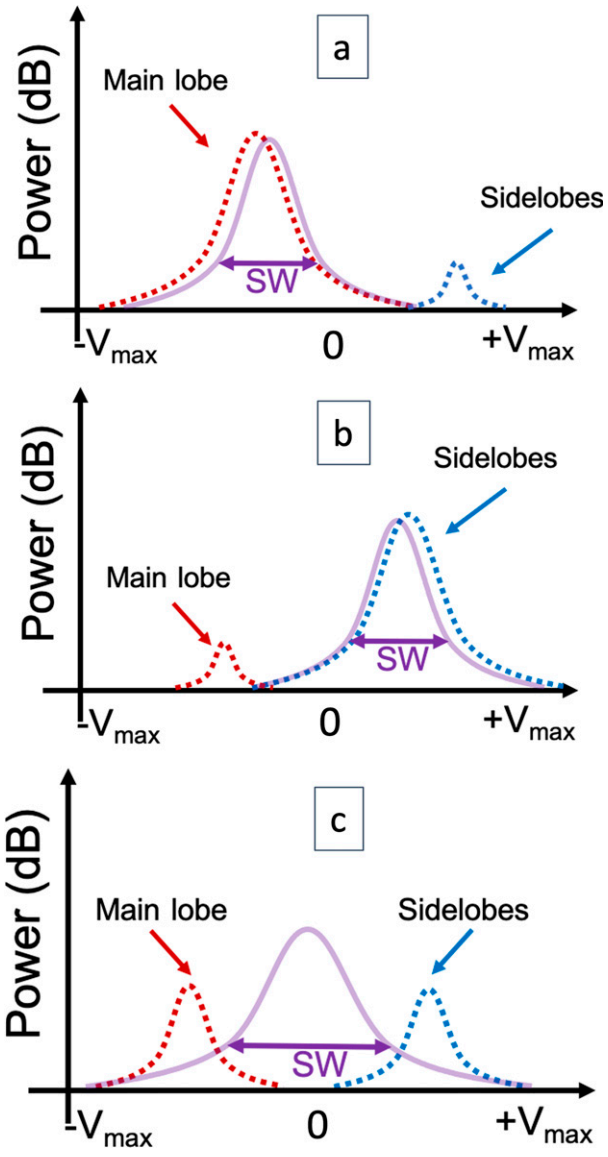

FIG. 6. Idealized Doppler power spectra showing main lobe returned power (red dashed curve), cumulative sidelobe returned power (blue dashed curve), and returned power mix (purple solid curve). Amplitude of dashed curves are not to scale, and their separation is for clarity. Dark purple double arrow denotes the relative span of SW. (a) Common scenario of the main lobe and sidelobe returned power mix in the absence of large Z gradients, valid for most weather events. (b) Extreme scenario that only occurs in the presence of extreme Z gradients where sidelobe returned power dominates. (c) Intermediate scenario where the main lobe and sidelobe returned power are about equal.

the 0.5° low-level, clear-air inflow region (soft white circle in Fig. 5b), there is an extensive and deep storm overhang with high dBZ (e.g., >50) aloft. The white shaded arc spanning approximately 135° within this overhang identifies the high dBZ values derived from high returned power within and well beyond the vertical plane at multiple elevations (up through 12.5°) that are sampled by the sidelobes. This cross section is built from volume coverage pattern (VCP) 12, a sequence of 14 predefined elevation angles sampled as full 360° rotations (Brown et al. 2005b). VCP 12 is designed for sampling severe convection and a "volume scan" takes up to five minutes to complete. Thus, Fig. 5b does not represent exactly what the antenna pattern samples when the main lobe is pointing at the lowest elevation. However, it is sufficient to demonstrate that supercell low-level regions of relatively low reflectivity are surrounded on the sides and top by regions of relatively high reflectivity, possibly yielding ESLC. The returned power from multiple sidelobes striking an extensive overhang is cumulative, equal to or dominating the returned power from the main lobe sampling the lowest elevation. The cross-section visualization technique in Fig. 5b and the schematic in Fig. 3c are proposed as a conceptual model for the source of ESLC.

Another tool for a qualitative understanding of ESLC is the Doppler power spectrum, which is the power-weighted distribution of V from the scatterers in the resolution volume. It is a representation of the returned power distribution for a given range gate and can be approximated by a Gaussian curve. It was not possible to obtain the raw time series or in-phase and quadrature-phase (IQ) data (Doviak and Zrnić 1984) for the cases in our study and thus calculate their Doppler spectra. The following Doppler power spectrum graphics represent concepts of the relative mix of returned power from the main lobe compared to that from all the sidelobes. They are idealized (i.e., not to scale) scenarios that are used herein to illustrate these concepts as they relate to the varying ways ESLC manifests in the data.

a. *Common scenario*

The Doppler power spectrum in Fig. 6a is valid nearly all the time for the WSR-88D. In the absence of large Z gradients, the main lobe returned power (red dotted curve) dominates that from the sidelobes (blue dotted curve). For the WSR-88D antenna pattern's first sidelobe, the two-way cumulative transmitted power is dramatically lower than the main lobe (−58.07 dB for KOUN). There is additional returned power from the other sidelobes, but the cumulative returned power is likely to remain $\sim 10^{-6}$ (linear scale) compared to that from the main lobe. The soft purple curve is a representation of the Doppler power spectrum, from which Z, V, and SW are extracted for the range gate. In the absence of large Z gradients with potentially severe convection, the soft purple curve closely represents the curve for the main lobe.

b. *Extreme scenario*

Opposite from the common scenario, and only possible in the presence of the largest Z gradients, is the cumulative sidelobe returned power dominating the returned power from the main lobe, shown in Fig. 6b. In this case, the Doppler power spectrum, from which Z, V, and SW are extracted for the range gate, more closely represents the returned signal from the sidelobes. The storm mode most capable of producing this extreme mix of returned power with time continuity is the supercell.

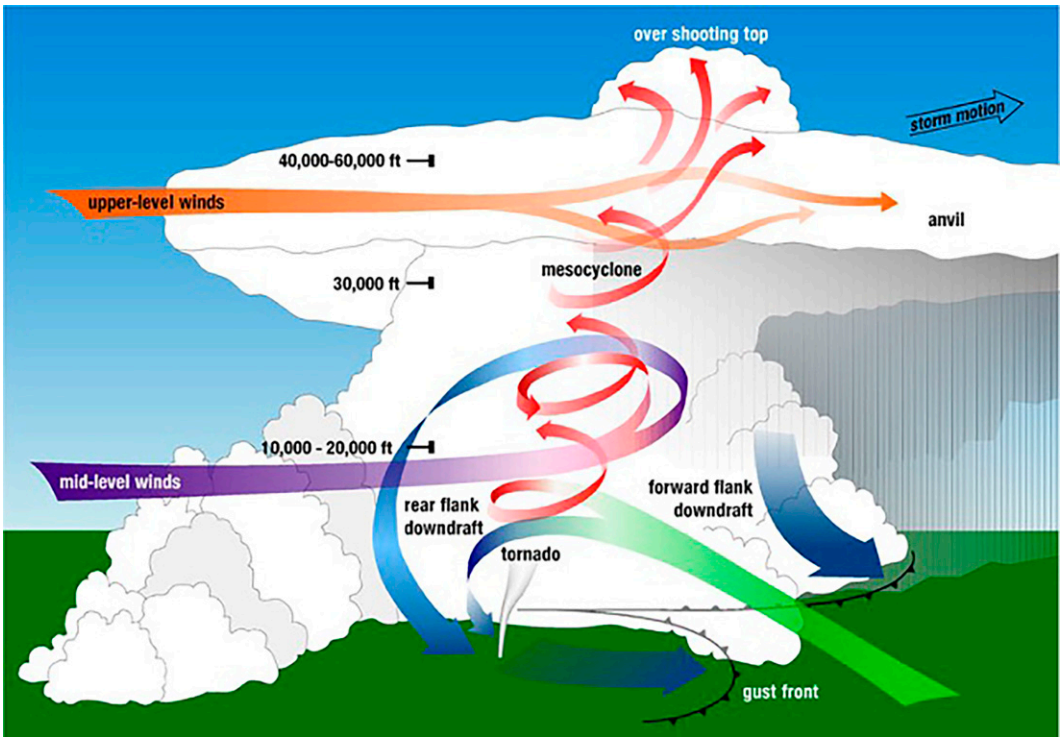

FIG. 7. Schematic of supercell wind trajectories with a typical wind direction in the low levels nearly opposite from that of the midlevels (courtesy NOAA/NSSL).

Considering that without large Z gradients, the WSR-88D antenna pattern results in returned power from the main lobe that is much greater ($\sim 10^6$) than that returned from the sidelobes, Fig. 6b would produce the rarest example of ESLC. The resultant field of SRV is smooth (i.e., not noisy), and SW is low. The authors present a particularly clear case in section 4, with these SRV and SW characteristics, thus suggestive of the returned power mix in Fig. 6b.

c. *Intermediate scenario*

From the perspective of possible power distributions between the main lobe and the sidelobes, there is an intermediate case. In Fig. 6c, the returned power from the main lobe and from the sidelobes are approximately equal. The respective velocities are displaced from one another, broadening the distribution and thus increasing the SW. Though the extent of the vertical wind shear varies, it is typical for a supercell to exhibit radial V in the low-level inflow region in the direction opposite that of the V in the echo overhang aloft (Fig. 7, courtesy NOAA/NSSL). Thus, the main lobe and sidelobe power-weighted V with directions opposite from one another broaden the SW for that range gate. In Fig. 6c, the magnitude of the wind speed for the main lobe and sidelobe returns is roughly equal, though this varies depending on the magnitude of the vertical wind shear near and within the supercell. For the remainder of this paper, Figs. 6b and 6c are sometimes referenced with the WSR-88D cases to support a qualitative, conceptual understanding of the resulting data.

In the context of supercells, the magnitude of the SW in ESLC can be affected by the extent of vertical wind shear within a supercell. However, vertical wind shear varies significantly within the broad category of supercells, and the authors do not wish to suggest to NWS warning forecasters that considering vertical wind shear is going to be helpful in diagnosing ESLC. It is sufficient to remember that the direction of radial V at low levels is likely to be opposite from that of the midlevels (Fig. 7), which contributes to a broadening of the SW, meaning that often (but not always), the SW is high when ESLC is present.

When there is sufficient returned power from the sidelobes, the most consequentially affected radar variables are SRV and SW, followed by CC. Within the low reflectivity regions adjacent to the storm's forward flank nearly all the ESLC cases from our study present noisy CC values lower than the threshold for nonmeteorological scatterers (i.e., <0.85; Kumjian 2013), while in rare cases, the CC values are still noisy, but suggestive of hail or graupel (i.e., 0.60–0.99; Kumjian 2013). These overlapping CC thresholds are based on S-band radar systems, and strategies for discriminating hail characteristics such as size or wetness, require other dual-polarization variables, such as differential reflectivity (Z_{DR}) and specific differential phase (KDP). For the purpose of identification of ESLC, CC is supportive due to noisiness and the frequent indication of nonmeteorological scatterers. However, the authors have found some exceptions with higher CC presented in this paper, which we speculate is due to a predominance of hail within the updraft and supercell overhang.

For the KBOX 4 August 2015 supercell from Fig. 5, the resultant ESLC at 0.5° is depicted in the circled area in Fig. 8,

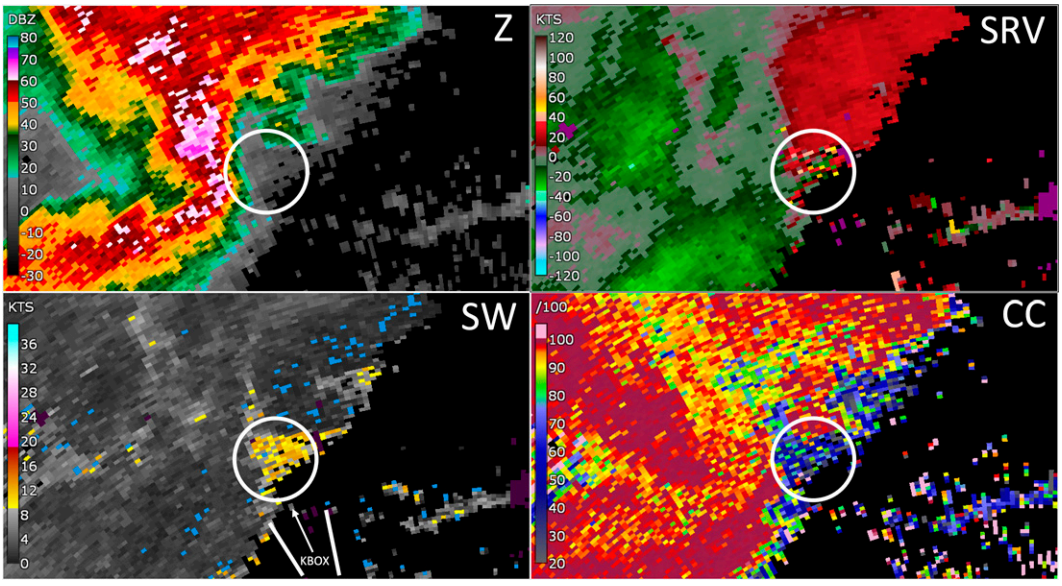

FIG. 8. Radar data from KBOX 1949 UTC 4 Aug 2015 with 0.5° (top left) Z, (top right) noisy SRV, (bottom left) high SW, and (bottom right) low CC in the low-level inflow region due to ESLC. The radar location and viewing angle is shown in the bottom-left panel.

with noisy SRV, high SW, and noisy, nonmeteorological CC in the low-level inflow region. The noisy SRV data and the high SW suggest a returned power distribution somewhat like Fig. 6c. Based on Nai et al. (2020), ESLC as presented in Fig. 8 is common, though it is often visually discarded by trained meteorologists accustomed to mentally filtering noisy data. Thus, it is "hiding in plain sight," meaning these data are seen, but not recognized as ESLC since additional evaluation of its source is commonly unnecessary given the insignificance of these noisy data.

This comparison of data from Z, SRV, SW, and CC is used for the remainder of our ESLC examples. The comparison process is defined as "sensemaking" by Klein et al. (2006) as "a motivated effort to understand connections … in order to anticipate their trajectories and act effectively." This captures how the identification of ESLC relies on multiple radar variables within the broader context of supercell storm interrogation. Though other radar variables, such as Z_{DR} and KDP, are available, the combination of Z, SRV, SW, and CC was most reliable for identifying ESLC in our study. None of these radar images alone can definitively identify ESLC, but their combination supports the NWS warning forecaster sensemaking process in real time.

The most consequential manifestation of ESLC is an apparent circulation, which introduces a significant cognitive challenge for the NWS warning forecaster during real-time warning operations. The conceptual model from the cross-section visualization in Fig. 5b and schematic in Fig. 3c, the Doppler power spectra in Figs. 6a–c, and diagnostic tools presented in sections 3 and 4 of this paper, are intended to support the NWS warning forecaster, and inform all WSR-88D users. Through this study, the authors have found that ESLC manifests in a variety of ways, of which apparent circulations are a small, but critical subset.

3. Examples of elevation sidelobe contamination, including apparent circulations

A Bentley et al. (2021) study of 6882 tornado warnings showed that tornado warning verification metrics (specifically FAR) performed significantly worse when V contamination (estimated to be 85%–90% sidelobe contamination) was present than when there was none (Fig. 9). Bentley et al. (2021) found that tornado warnings issued when V contamination was present had a FAR of 0.79 compared to 0.66 when there was no V contamination present. In addition, the frequency of contaminated V was at a maximum between 1.2 and 2.4 km (4 and 8 kft) ARL, which suggests a preferred location for storm range and height such that the main beam is sampling clear air in the low-level inflow region, while the sidelobes are sampling the echo overhang and returning significant power compared to the main lobe. Correct identification of these contaminated velocity signatures offers a unique opportunity to reduce the NWS tornado warning FAR without also reducing the POD. The recognition and diagnostic techniques presented in this paper support this identification in real time. This section presents a series of examples of ESLC as a first step in the familiarization and recognition process.

a. *Blend of TBSS and ESLC*

Depending on storm orientation with respect to the radar, an intense hail core at low levels and aloft can result in a blend of a TBSS and ESLC. Figure 10a [Albany, New York (KENX), 15 May 2018 at 0.5°] depicts a supercell southeast of the radar. Very high reflectivity (60–75 dBZ) along the storm's forward flank is indicative of hail. There is enhancement of

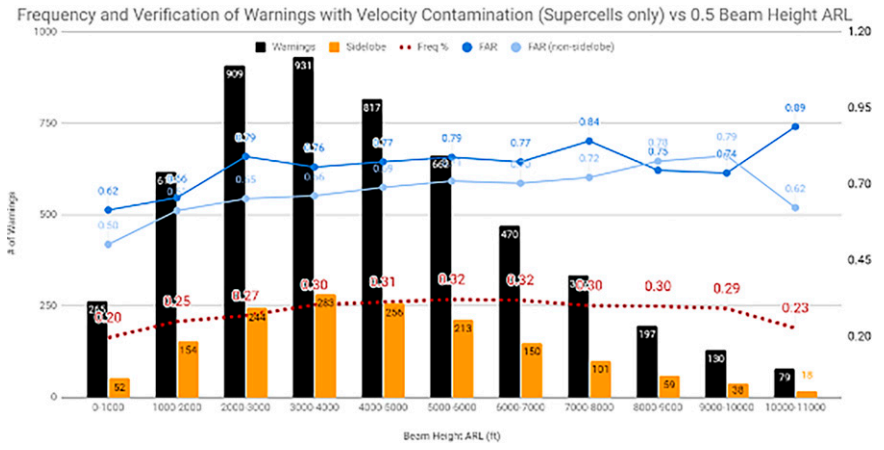

FIG. 9. Chart from Bentley et al. (2021) showing the frequency and verification of tornado warnings with velocity contamination present at 0.5° beam height ARL (ft).

dB*Z* in the clear-air region down radial from the storm core, as is often seen with a TBSS. There is a slight difference in the SRV and SW fields, on either side of the dashed white line in Fig. 10a that roughly bisects the TBSS. On the western portion of the TBSS, the SRV field is a little noisier and the SW field is higher than on the eastern portion of the TBSS. In Fig. 10b, the cross section from the antenna perspective reveals a significant difference in the dB*Z* gradients at elevations above the respective portions of the TBSS at 0.5°, with lower dB*Z* gradients aloft on the western portion compared to the eastern potion. At 0.5° in Fig. 10a, the western portion depicts noisier SRV and higher SW, suggesting ESLC with a main lobe and sidelobe retuned power mix closer to Fig. 6c. The eastern portion depicts smoother SRV and lower SW (beige arrow) suggesting ESLC with a main lobe and sidelobe retuned power mix closer to Fig. 6b, due to the higher returned power from the sidelobes from the highly reflective hydrometeors aloft. For operational purposes, this example is included to demonstrate that due to storm orientation, a blend of TBSS and ESLC is possible. In the absence of circulations that may develop, the TBSS is the more operationally relevant feature, increasing confidence in large hail at the 0.5° elevation and aloft.

This potential manifestation of ESLC within the TBSS swath at 0.5° in Fig. 10 is not presented with an expectation of recognition during real-time warning operations. The intention aligns with the discovery as another way ESLC appears in the data as "hiding in plain sight." In the context of NWS warning operations, the significance of the TBSS is appropriately recognized, increasing confidence in the presence of large hail. Both the TBSS and ESLC commonly appear along the supercell's low-level forward flank, sometimes in close proximity to the supercell hook region, requiring scrutiny for the development of circulations, which may be valid or imposters. The remainder of this paper focuses on strategies for identifying imposter circulations due to ESLC.

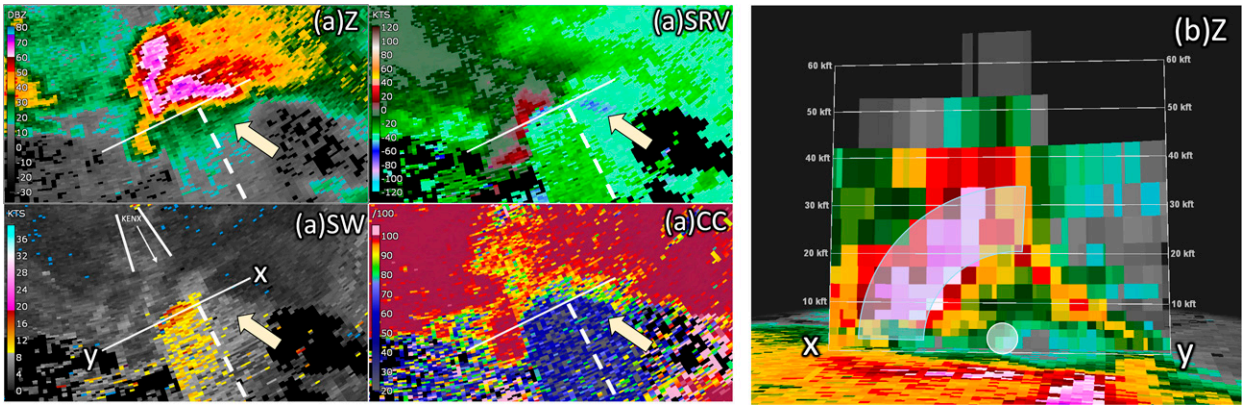

FIG. 10. Radar data from KENX 1845 UTC 15 May 2018 (a) 0.5° with a blend of ESLC and a TBSS. The white dashed line roughly bisects the TBSS, with a possible contribution from sidelobe contamination within the eastern half of the TBSS (beige arrow); (b) cross section along the white line left to right normal to the outgoing radar beam in (a) with the shaded arc revealing the extent of highly reflective hydrometeors aloft that the sidelobes encounter.

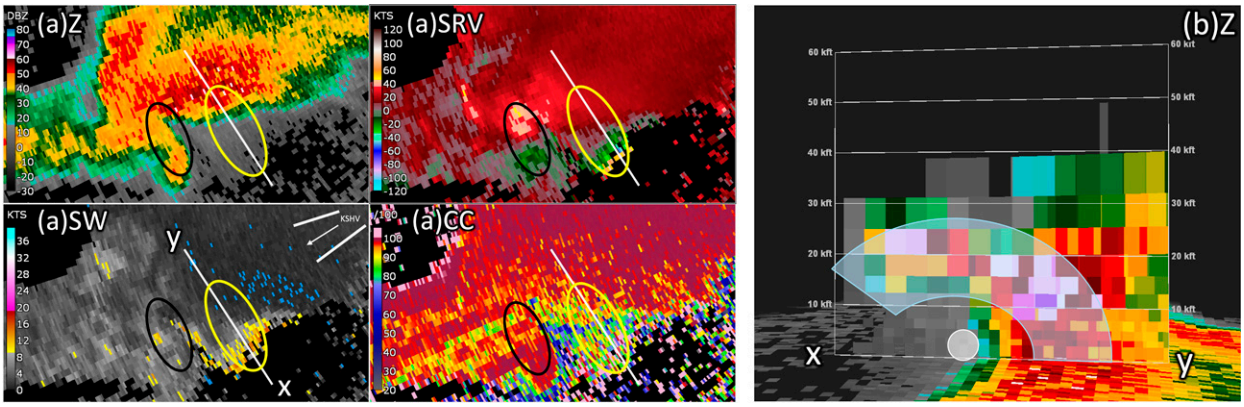

FIG. 11. Radar data from KSHV 0027 UTC 21 Oct 2019 (a) 0.5° well separated imposter circulation due to ESLC (yellow oval) and a valid circulation (black oval); (b) cross section along the white line left to right normal to the outgoing radar beam in (a) with the shaded arc revealing the extent of highly reflective hydrometeors aloft that the sidelobes encounter.

b. *Valid circulations coexisting with imposters*

Smith et al. (2012) showed that 71.8% of all tornadoes were produced by supercells, thus properly diagnosing imposter circulations within supercells is very important for effective analysis of potentially tornadic storms. Increased confidence in the validity (or lack thereof) of circulations will greatly help those who are tasked with issuing tornado warnings. Further, Bentley et al. (2021) showed the degradation on warning performance when V contamination (the majority of which was ESLC) was present. Though rare, our study includes cases with an imposter circulation due to ESLC coexisting with a valid circulation presented here to illustrate the differences in appearance. The coexisting imposter and valid circulations comprised 11.1% of all the Bentley et al. (2021) cases with velocity contamination. Here, we focus on these examples to reinforce the most important tool for diagnosing imposter circulations: location.

When faced with both a valid and an imposter circulation, calculating the rotational velocity (V_{rot}; Thompson et al. 2017) from the valid circulation is critical. Strong midlevel wind speeds and strong midlevel rotation are commonly associated with supercells. Therefore, when these stronger velocities are superimposed at a lower elevation due to sidelobe contamination, they often appear with V_{rot} in excess of 30 kt (1 kt ≈ 0.51 m s^{-1}), which is the baseline tornado warning guidance from the Warning Decision Training Division (WDTD 2021). For example, a valid circulation can exhibit a V_{rot} of 10–15 kt, while the imposter circulation is showing a V_{rot} of 35–40 kt. This stronger imposter circulation can easily distract from the valid circulation and lead to an incorrect analysis of the tornado threat. Decision-making based on imposter circulations potentially affects the timing of the initial tornado warning issuance, impacts tags (i.e., "considerable" or "catastrophic"; WDTD 2021) within the warning, and messaging within follow-up statements. The next three examples explore the dilemma of coexisting valid and imposter circulations. The texture (i.e., noisiness) of the SRV fields and the magnitude of SW is discussed, as these clues support both the existence of an ESLC imposter circulation and the possible mixes of returned power from the main lobe compared to the sidelobes suggested by Fig. 6b or Fig. 6c.

Figure 11a from Shreveport, Louisiana (KSHV), 21 October 2019 at 0.5° depicts both an imposter circulation due to ESLC and a valid circulation that are widely spaced (10.7 km or 5.8 n mi), and the location with respect to Z clarifies the difference. The valid circulation is collocated with sufficient dBZ values (i.e., typically >20 dBZ) and a hook (black oval). The imposter due to contamination (yellow oval) has an inbound SRV component that lacks a clear maximum (including a few gates with dealiasing errors on the outer edge) entirely within the clear air adjacent to the low-level storm inflow. The contamination is relatively easy to identify due to the noisy texture of the SRV and the high SW, suggesting a returned power mix from the main lobe and the sidelobes similar to Fig. 6c, also supported by the cross section in Fig. 11b. This case depicts an imposter circulation that is conspicuous to most radar users due to the location and texture of the SRV. Despite the presence of an imposter circulation, there is still a valid case for a tornado warning as the real circulation is collocated with the Z hook and exhibits a V_{rot} of ~32 kt. However, characteristics of the warning such as polygon placement and expiration time rely on identification of the valid circulation.

Compared to the storm in Fig. 11a, the supercell in Fig. 12a [Bismarck, North Dakota (KBIS), 12 August 2017 at 0.5°] has an imposter circulation and a valid one closer together (2.9 km or 1.6 n mi). The sufficient dBZ values and a hook structure confirm which of the circulations is valid (black oval). The imposter due to ESLC (yellow oval) has a block of inbound SRV with noisy texture, located in the low-level clear air adjacent to the storm inflow. It lacks an inbound maximum unlike the valid circulation in the hook echo. The radar is to the north-northeast, and the orientation is such that there is a wide TBSS down radial from the hook and the forward flank, which partly contributes to the returns within the low-level storm inflow region. Thus, the TBSS is also likely contributing to the inbound SRV values within the imposter circulation. In Fig. 12b, the intensity of dBZ aloft suggests highly reflective hydrometeors and high cumulative returned power from the

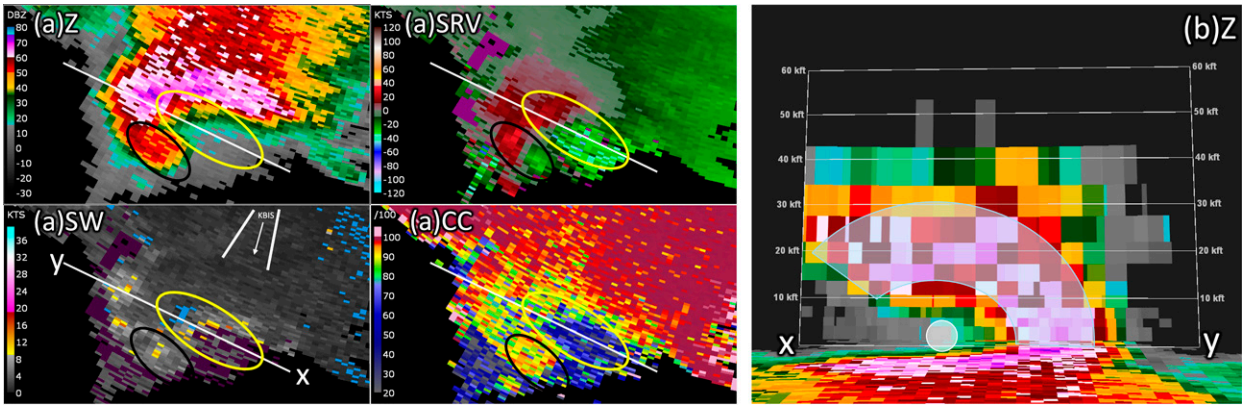

FIG. 12. Radar data from KBIS 2349 UTC 12 Aug 2017 (a) at 0.5° ESLC (yellow oval) and a valid circulation (black oval) in close proximity; (b) cross section along the white line left to right normal to the outgoing radar beam in (a) with the shaded arc revealing the extent of highly reflective hydrometeors aloft that the sidelobes encounter.

sidelobes. The strong dBZ aloft revealed by the cross section and the low SW suggests a main lobe and sidelobe returned power mix similar to Fig. 6b. However, the slight noisiness of the SRV field suggests a main lobe and sidelobe returned power mix similar to Fig. 6c. Without the ability to acquire the IQ data and verify through signal processing, the best qualitative conclusion is that the main lobe and sidelobe returned power mix is somewhere between Figs. 6b and 6c with contributions from the TBSS and the ESLC. The V_{rot} for the potentially tornadic circulation in the hook echo is ~32 kt while the V_{rot} would be ~40 kt if the contaminated inbound velocities were used in the rotational velocity calculation. This would result in an overestimation of the probability of tornado occurrence by 13% (36% versus 23%; Thompson et al. 2017).

Figure 13a from Jackson, Mississippi (KDGX), 15 February 2016 depicts the 0.5° elevation angle and exhibits an imposter circulation (yellow oval) and a valid one (black oval) within 3.7 km (2 n mi) of one another. The radar is north-northeast of the storm. The valid circulation is collocated with sufficiently high reflectivity factor (>20 dBZ) for confidence in main beam scattering, while the imposter's inbound component is an extended block located in the storm's very narrow inflow region. In this case, the imposter's inbound SRV exhibits low SW and has a smooth texture, lacking a well-defined speed maximum and radial wind speed gradient, unlike the valid inbound component. The cross section in Fig. 13b depicts an extensive overhang with multiple elevations spanning nearly 180° around the main lobe for the sidelobes to sample. Within the imposter circulation, the smooth SRV field and low SW suggest a main lobe and sidelobe returned power mix similar to Fig. 6b.

In Fig. 13, the valid and potentially tornadic circulation in the hook has a V_{rot} of ~40 kt, while the imposter circulation in the forward flank has a V_{rot} of ~60 kt. The probability of tornado occurrence (Thompson et al. 2017) is 41% for the valid circulation and 89% for the imposter, more than double the probability. Though other factors contribute, the decision to issue a tornado warning is supportable based on the valid circulation's V_{rot} and a 41% probability. The potentially negative implications of basing

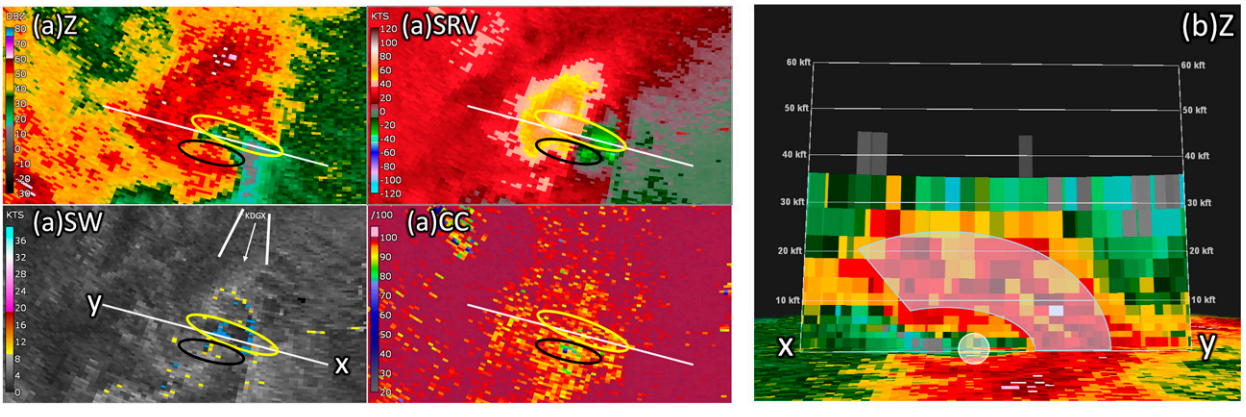

FIG. 13. Radar data from KDGX 1836 UTC 15 Feb 2016 (a) 0.5° close together imposter circulation due to ESLC (yellow oval) and a valid circulation (black oval); (b) cross section along the white line left to right normal to the outgoing radar beam in (a) with the shaded arc revealing the extent of highly reflective hydrometeors aloft that the sidelobes encounter.

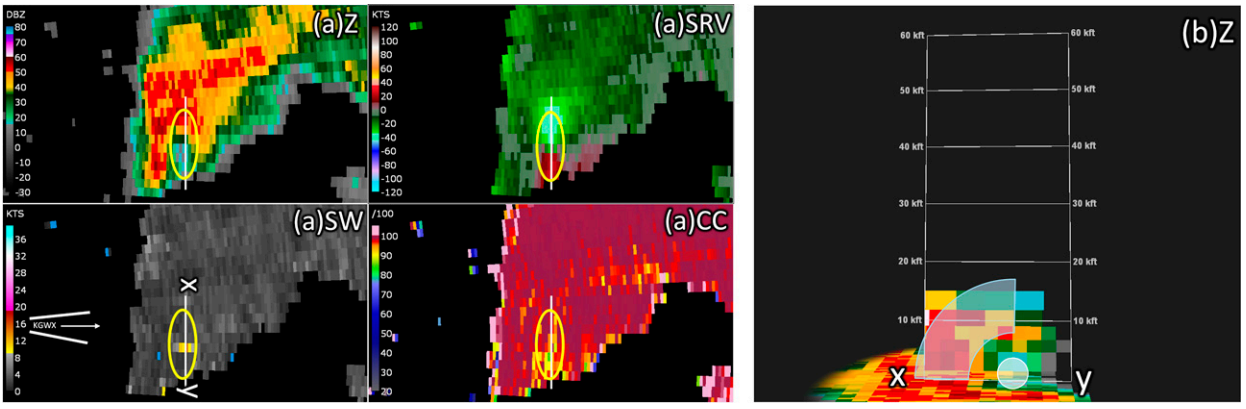

FIG. 14. Radar data from KGWX 2107 UTC 23 Feb 2019 (a) 0.5° apparent circulation for a mini-supercell (yellow oval), with the outbound component located in the clear-air inflow region; (b) cross section along the white line left to right normal to the outgoing radar beam in (a) with the shaded arc revealing the extent of highly reflective hydrometeors aloft that the sidelobes encounter.

the warning decision on the imposter and its associated V_{rot} would be incorrect warning polygon placement and expiration time, in addition to an incorrect impact-based warning tag. The impact-based warning tags serve as modifiers for the tornado warning. Based on WDTD Impact Based Warnings (IBW) guidance (WDTD 2021), the imposter circulation with a V_{rot} of ~60 kt warrants a "considerable" tag, while the valid circulation with a V_{rot} of ~40 kt is borderline for a "considerable" tag (both of which also require a verifiable tornado in progress). As NWS forecasters strive toward more accuracy related to potential tornado intensity as part of warning decision-making, distinguishing valid from imposter circulations can support this effort.

c. *Difficult-to-diagnose case*

The authors do not suggest that this study has been exhaustive, and there are inevitable borderline cases when radar sampling is compromised due to either the range to a storm or its depth. As radar range increases, diagnosis techniques for apparent circulations can be less effective once the lowest elevation of a WSR-88D is sampling a midlevel mesocyclone rather than any low-level features. While midlevel mesocyclone behavior shows some predictive value for tornado potential (Thompson et al. 2017), the ability to discriminate between the mesocyclone and sidelobe contamination becomes less likely. Mini-supercells (American Meteorological Society 2022) are particularly challenging as range from the radar increases, making it difficult to determine if an apparent circulation is ESLC or if the midlevel mesocyclone is being sampled. The relative shallowness reduces confidence of ESLC based on the cross-section visualization technique, while the sensemaking approach related to expected storm structure can increase confidence. This dilemma is explored with Fig. 14, which we believe is an example of ESLC, though more consideration and conversation was required compared to the other examples in this paper.

Figure 14a depicts a mini-supercell from Columbus Air Force Base, Mississippi (KGWX), 23 February 2019 at the 0.5° elevation angle, at a range of 85 km (46 n mi) east of the radar, with a storm top of 4.6 km (15 kft). There is a distinct inflow notch with a block of outbound SRV implying a possible circulation (yellow oval). However, the location of the outbound SRV and the lack of a maximum supports ESLC. Most notably, the outbound SRVs only appear in the inflow notch where reflectivity is mostly below 20 dBZ, implying that the outbound SRVs are anomalously associated with lower returned power, which hints at ESLC. There is an appendage in Z that is the expected location for a valid circulation. The cross section in Fig. 14b reveals a modest overhang and broad updraft region. For this case, the storm overhang is modest compared to other examples in this paper, while the breadth of the updraft region is the primary source of highly reflective hydrometeors for the sidelobes to strike. This differs from the more typical (and easier to diagnose) supercells from our study, and examples presented herein. The low SW in Fig. 14a associated with the relatively smooth outbound SRV field is inconsistent with the expected moderate contribution of sidelobe returned power based on Fig. 14b. However, the low topped nature of this supercell, relative lack of high (>60 dBZ) reflectivity, and generally high CC suggests that it has few hydrometeors composed of ice (Kumjian 2013), thus a lower diversity of scatterers moving with the mean flow. Ultimately for this case, location is the most compelling factor supporting the conclusion of ESLC. The location of the block of outbound SRV lacking realistic texture within an area of low dBZ does not make sense, and the apparent circulation is more likely to be ESLC than some portion of the storm's mesocyclone.

This section provides examples of varying types of ESLC, in order to grow awareness for all users, and especially NWS warning forecasters. Beyond the most common low-level clear-air inflow region of noisy SRV, high SW, and low CC (Fig. 8), storm orientation can result in a blend of a TBSS and ESLC. When blended with a TBSS, this contamination remains "hiding in plain sight." and is likely mentally filtered by users. The TBSS is the more important feature, since it increases confidence in the presence of large hail. However, both the TBSS and the ESLC can potentially interfere with the tornado warning decision-making process. The most consequential type of ESLC is an apparent circulation, requiring cognitive resources to diagnose. The coexisting valid and imposter circulations stress the importance of

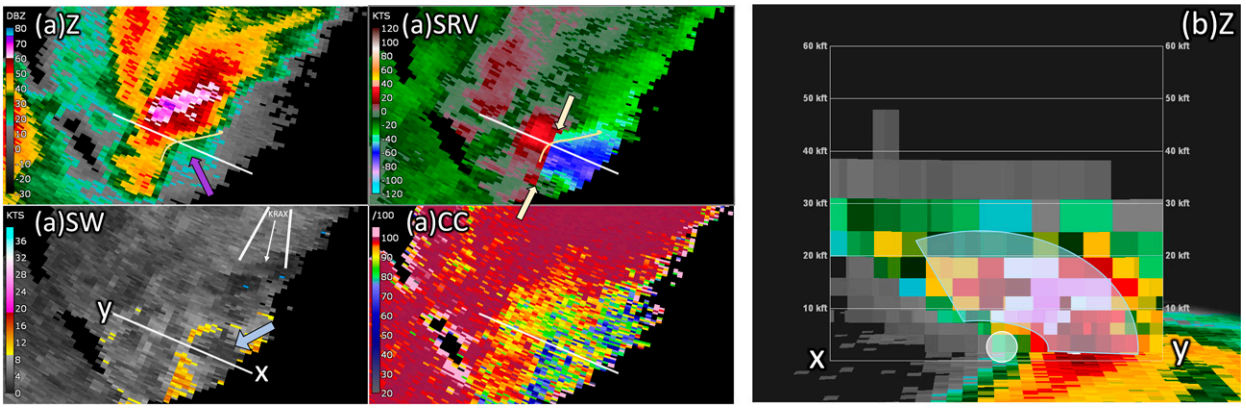

FIG. 15. Radar data from Raleigh–Durham, NC (KRAX), 2222 UTC 24 Feb 2016 (a) at 0.5° with an apparent circulation; note the location (bounded by the beige curve) and lack of a maxima structure of the suspect inbound component, the unrealistically extensive azimuthal shear (beige arrows), the dBZ enhancement in the low-level inflow region (purple arrow) and the low SW (blue arrow); (b) cross section along the white line left to right normal to the outgoing radar beam in (a) with the shaded arc revealing the extent of highly reflective hydrometeors aloft that the sidelobes encounter.

location as a diagnostic tool. Section 4 provides a comprehensive look at all the apparent circulation diagnostic tools the authors have thus far discovered.

4. Apparent circulations: How to diagnose validity

The previous series of ESLC examples was presented to demonstrate the different manifestations of ESLC, from noisy data in the storm inflow region to apparent circulations. In parallel, diagnostic tools were introduced. This section provides a closer look at all elements known by the authors to aid forecasters in the sometimes-difficult task of diagnosing and identifying imposter circulations. Given the potential for improving NWS warning performance by lowering FAR without negatively impacting POD, the diagnostic tools are given a special emphasis in this section.

The authors have found that the most reliable technique for identifying imposter circulations is to closely evaluate the location of such a circulation with respect to the forward flank. This is reasonable as it supports our sensemaking with respect to the conceptual model of supercell structure (Browning 1964; Doswell and Burgess 1993; Lemon and Doswell 1979). Valid tornadic circulations are most frequently beneath the updraft on the leading edge of the rear-flank downdraft (RFD), typically near the tip of reflectivity within the hook echo. Often, imposter circulations appear along the forward flank in the inflow region of a supercell, an area that is typically free of precipitation. Given sufficient depth of highly reflective hydrometeors within the storm overhang, returned power within the low-level inflow can be dominated by that from the sidelobes, even increasing low-level clear-air values to 20–25 dBZ. The transition zone between the low-level inbound and outbound velocities in this region can be unrealistically abrupt along the leading edge of the forward flank, as in Fig. 15. Another clue that is often present is that the SRV field in the inflow has an overall blocky texture, lacking the typical structure with a maximum within the inbound or outbound component of a valid circulation (Fig. 2). While it is possible to notice discrepancies such as SRV texture, which likely indicate the presence of ESLC, the location of the circulation remains the most obvious discriminator. At times, interrogation of multiple adjacent radars can be utilized to help diagnose imposter circulations, such as WSR-88Ds or Terminal Doppler Weather Radar (TDWR). However, the majority of these imposter circulations happen below 1.8 km (6 kft; Bentley et al. 2021) and radar coverage from multiple WSR-88Ds below 1.8 km (6 kft) is quite rare.

A final example is presented here as a collection of all the diagnostic data cues yet identified through this study, including but not limited to location. The supercell in Fig. 15 is south-southwest of the radar site and exhibits an apparent circulation that persisted for nearly one and a half hours (2147–2311 UTC). The SW associated with the block of smooth inbound SRV values is low (blue arrow), implying a significant contribution of cumulative returned power from the sidelobes, compared to that from the main lobe (Fig. 6b), which is supported by the cross section in Fig. 15b. Also note the enhanced dBZ values (~20–25) in the low-level clear-air inflow region (purple arrow). While some limited three-body scattering may be contributing, the lack of a down-radial extension of noisy SRV, high SW, and very low CC do not suggest a TBSS. It is far more likely that the enhanced dBZ is due to returned power from the sidelobes.

In Fig. 15a, there are multiple diagnostic data cues that reveal this circulation to be an imposter. Starting with location, the entire inbound component of this apparent circulation lies in the low-level clear-air inflow region of the supercell (bounded by the beige curve). As with the multiple previous imposter circulation examples, the location of one component of the Fig. 15 circulation entirely within the storm inflow region conflicts with the conceptual model of a valid circulation with a supercell. Also note the texture of the SRV field throughout the suspect inbound component. There is a large block of range gates with ~50–60-kt inbounds extending to the outer edge of the clear-air inflow region, lacking the structure

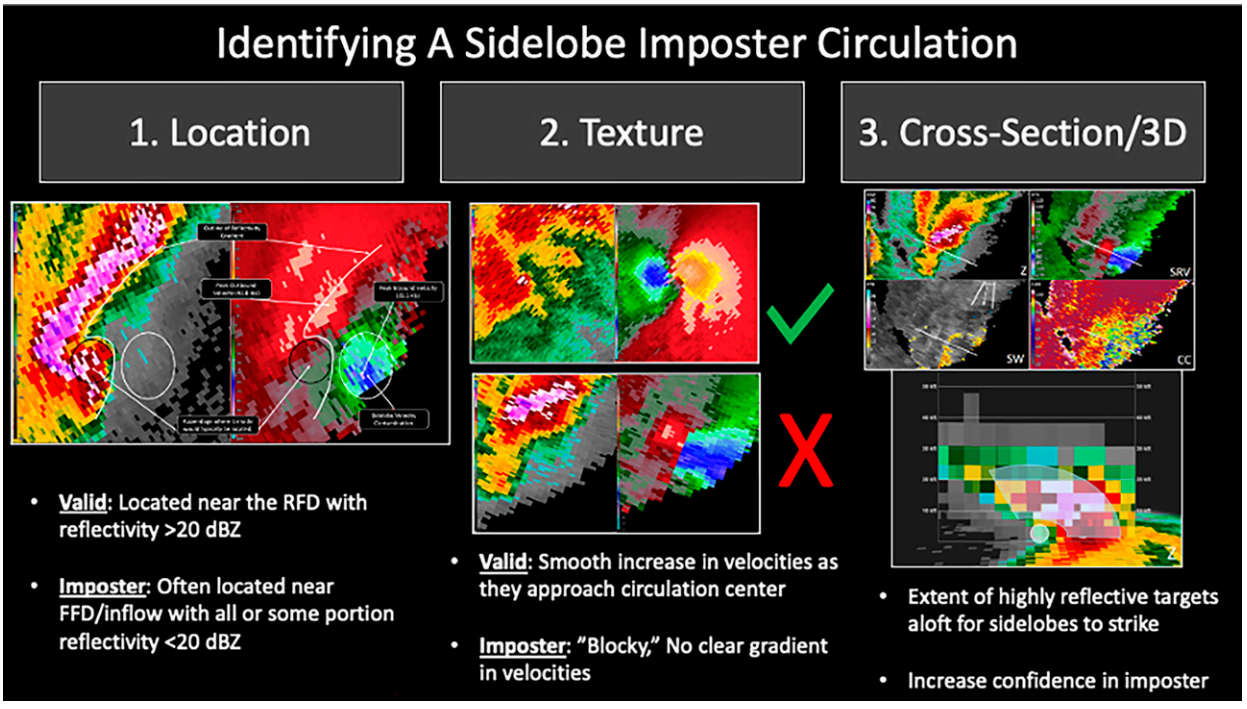

FIG. 16. Summary of the diagnostic process for determining the validity of an apparent circulation, from location to texture of the velocity field to the cross-section technique for increased confidence of ESLC.

of a valid inbound portion of a circulation (Fig. 2). In SRV, there is extreme shear between adjacent azimuth angles over a significant radial extent, indicated by the beige arrows. This unrealistic shear has not been mentioned in the previous examples presented in this paper but has been observed in other cases. Though gate-to-gate azimuthal shear can be important for circulation identification, the extended azimuthal shear in Fig. 15a conflicts with our sensemaking process for valid circulation structure (Fig. 2). In addition to location, the SRV texture and the extensive azimuthal shear fail the conscious and sometimes unconscious sensemaking processing for NWS warning decision forecasters, increasing confidence that this apparent circulation is an imposter.

Figure 16 summarizes the characteristics of this diagnosis process when faced with an apparent circulation. The first step is to consider the location of all or part of the circulation with respect to the RFD, forward-flank downdraft (FFD) or inflow region, and the collocated reflectivity values. Valid circulations are typically located within the RFD with reflectivity > 20 dBZ. All or some portion of an imposter circulation is typically located adjacent to the FFD or inflow region with reflectivity < 20 dBZ. Further, the texture of the SRV field can support (typical gradient and maxima structure) or refute (blocky without maxima structure) the validity of the apparent circulation. Finally, drawing a cross section from left to right normal to the radar-viewing angle reveals the storm structure above the lowest radar elevation. The extent and intensity of the overhang can increase confidence that the apparent circulation is the result of ESLC, and it is an imposter.

5. Summary

The varying types of WSR-88D sidelobe contamination are summarized in Table 1. The most easily understood and

TABLE 1. Summary of sidelobe contamination types.

Sidelobe contamination type	Z gradient source	Sidelobe contamination subtype	Manifestation in base data	Operations impact
Azimuthal	Apparent on same PPI scan		Azimuthal extension in clear air adjacent to storm core	Minimal
Elevation	Not apparent without cross section	Most frequent	Noisy V, high SW, low CC	Minimal
		Rare	Apparent circulation in V	Major
		w/TBSS	TBSS dominant	Either ESLC or TBSS could potentially obscure a circulation

recognized form is azimuthal sidelobe contamination. This is usually associated with a strong hail core and can be observed at any radar elevation angle that is sampling the hail core. It is readily identified near the dBZ gradient on the same elevation scan and can often increase confidence in the presence of large hail. The focus of this paper is on a different, and far more consequential, form of sidelobe contamination. As the main lobe is sampling the low levels of a supercell, our cross-section technique allows for a visualization of the extent of highly reflective hydrometeors aloft sampled by the sidelobes. Combined with the schematic in Fig. 3c, this conceptual model depicts the multiple elevations sampled by the sidelobes pointing in all directions away from the main lobe. The relative mixes of returned power from the main lobe and the sidelobes (Fig. 6) can contaminate the radar base data, especially SRV and SW.

ESLC appears in a variety of ways in the low-level radar images, and supercells are the most likely storm mode to produce it. The majority of ESLC in the WSR-88D "hides in plain sight," as its characteristics are noisy SRV, high SW, and low CC in the low-level, typically clear-air inflow region. However, there are exceptions when SRV can be smooth, SW can be low, or CC can be suggestive of hail. Another type of "hiding in plain sight" is due to a radar-relative storm orientation such that ESLC blends with a TBSS, and contamination effects observed within the TBSS are typically subtle. The most consequential form of ESLC is an apparent circulation and its impact on NWS warning performance.

Simmons and Sutter (2009) showed the trade-off between POD and FAR on tornado fatalities and injuries is nearly equal, which makes reduction in FAR difficult given its direct correlation and the asymmetric penalty function (Brooks 2004) with missed events. However, Bentley et al. (2021) shows that tornado warnings issued when contaminated V is present have a FAR around 8%–10% higher than warnings issued in absence of contaminated V. This suggests that if NWS warning forecasters better understand and identify ESLC, some FAR reduction can be accomplished with minimal POD reduction. In addition to the potential for false alarm tornado warnings, misidentification can also result in incorrect V_{rot} calculations from imposter circulations that can then impact IBW warning tags on real circulations. All of these considerations do not change the importance of environmental parameters, as supercells in a favorable environment for tornadoes may still have a high tornado threat, along with the possibility of ESLC.

The authors have found the conceptual model from the cross-section visualization technique and Fig. 3c increases confidence in the presence of ESLC. Use of the cross-section technique for training and poststorm analysis is recommended to develop recognition of suspect data within a supercell's low-level inflow region in real time. It may not always be possible to use as a real-time tool for an NWS warning forecaster, but could be used by an additional team member, such as a warning forecaster assistant. Repeated exposure to the cross-section technique, along with the diagnostic data cues revealed in this paper, provide a foundation for identification of ESLC in real time. By knowing what to look for, NWS warning forecasters can recognize ESLC while using all-tilts radar display methods, which are typical for storm interrogation. Further, it is our experience that after repeated exposure to this conceptual model, recognition of potential ESLC also improves, starting with the 0.5° base data. Confidence then increases by quickly looking at the extent of echo overhang aloft, as part of routine storm interrogation of multiple elevations.

Diagnosis of an apparent circulation is best summarized as sensemaking. The most reliable tool is the location, which means a valid circulation is expected to be collocated with dBZ values that are at minimum, associated with precipitation (≥20 dBZ). In the rare examples of very low dBZ hook development, identifying a hooklike structure is still key. When all or part of an apparent circulation is located outside of the body of the supercell, especially in the low-level inflow adjacent to the forward flank, that circulation is suspicious. The structure or texture of the SRV field within a potential circulation's inbound or outbound component may be inconsistent with a valid circulation's appearance. There is sometimes an exaggerated extension of azimuthal shear from the inbound to outbound components of an apparent circulation. Finally, though the SW associated with ESLC is most often high, there are exceptions, likely due to a dominance of returned power from the sidelobes compared to the main lobe. Given these tools to raise awareness of what to look for with potentially tornadic supercells, there is an opportunity for increased recognition of imposter circulations in real time.

6. Future work

One desirable next step is an engineering collaboration to better understand the returned power mixture from the main lobe and the sidelobes with supercells. For example, though limited, there are cases of IQ data for supercells collected by the KOUN radar. Signal processing of these data could be performed to reveal the actual Doppler power spectra and the quantitative mix of the returned power from the main lobe and the sidelobes. A collection of these processed cases is expected to refine our understanding of storm characteristics that lead to, for example, low SW in the ESLC.

NWS forecaster real-time identification of ESLC could be supported by an automated decision aid. For example, a WSR-88D radar product generator (RPG) algorithm designed to identify possible ESLC could be developed. The sidelobe levels and azimuthal placement from the main lobe within the WSR-88D antenna pattern could support such an algorithm. The range gates with suspected ESLC could be identified by the algorithm and displayed as an overlay for velocity products, alerting the NWS forecaster to further interrogate the storm.

The recommendations for WSR-88D base data identification of ESLC documented here have been presented to a few NWS personnel thus far. Further presentations and discussions with NWS audiences of this consequential artifact are anticipated in the future. Another desirable goal to raise awareness is collaboration with the WDTD to help ensure NWS forecasters are best equipped to identify these features in their real-time methodologies.

Acknowledgments. The authors are grateful to Joseph C. Picca, James Ladue, Larry Hopper, and three anonymous

reviewers, who collectively greatly improved the quality of the manuscript. We are very grateful to Sebastian Torres for his considerable time and expertise in discussions about the core concepts behind the main lobe and sidelobe returned power combinations. Our thanks to David Schvartzman for graphics development support and his radar engineering review of the Doppler power spectrum section. We are grateful to Don Burgess for his very helpful discussions and recommendations for presenting the radar engineering concepts for a meteorological audience. A portion of the funding for this work was provided by NOAA/Office of Oceanic and Atmospheric Research under NOAA–University of Oklahoma Cooperative Agreement NA11OAR4320072, U.S. Department of Commerce.

Data availability statement. All the weather cases for this study are publicly available from the National Centers for Environmental Information (NCEI) WSR-88D level-II database, downloaded from Amazon Web Services: https://noaa-nexrad-level2.s3.amazonaws.com/index.html.

REFERENCES

American Meteorological Society, 2022: Mini-supercell. Glossary of Meteorology, https://glossary.ametsoc.org/wiki/Mini-supercell.

Andra, D. L., Jr., E. M. Quoetone, and W. F. Bunting, 2002: Warning decision making: The relative roles of conceptual models, technology, strategy, and forecaster expertise on 3 May 1999. *Wea. Forecasting*, **17**, 559–566, https://doi.org/10.1175/1520-0434(2002)017<0559:WDMTRR>2.0.CO;2.

Bentley, E. S., R. L. Thompson, B. Bowers, J. Gibbs, and S. Nelson, 2021: An analysis of 2016–18 tornadoes and National Weather Service tornado warnings across the contiguous United States. *Wea. Forecasting*, **36**, 1909–1924, https://doi.org/10.1175/WAF-D-20-0241.1.

Bluestein, H., C. Weiss, M. French, E. Holthaus, R. Tanamachi, S. Frasier, and A. Pazmany, 2007: The structure of tornadoes near Attica, Kansas, on 12 May 2004: High-resolution, mobile, Doppler radar observations. *Mon. Wea. Rev.*, **135**, 475–506, https://doi.org/10.1175/MWR3295.1.

Brooks, H. E., 2004: Tornado-warning performance in the past and future: A perspective from signal detection theory. *Bull. Amer. Meteor. Soc.*, **85**, 837–844, https://doi.org/10.1175/BAMS-85-6-837.

——, and J. Correia, Jr., 2018: Long-term performance metrics for National Weather Service tornado warnings. *Wea. Forecasting*, **33**, 1501–1511, https://doi.org/10.1175/WAF-D-18-0120.1.

Brotzge, J., and W. Donner, 2013: The tornado warning process. A review of current research, challenges, and opportunities. *Bull. Amer. Meteor. Soc.*, **94**, 1715–1733, https://doi.org/10.1175/BAMS-D-12-00147.1.

Brown, R. A., V. T. Wood, and D. Sirmans, 2002: Improved tornado detection using simulated and actual WSR-88D data with enhanced resolution. *J. Atmos. Oceanic Technol.*, **19**, 1759–1771, https://doi.org/10.1175/1520-0426(2002)019<1759:ITDUSA>2.0.CO;2.

——, B. A. Flickinger, E. Forren, D. M. Schultz, D. Sirmans, P. L. Spencer, V. T. Wood, and C. L. Ziegler, 2005a: Improved detection of severe storms using experimental fine-resolution WSR-88D measurements. *Wea. Forecasting*, **20**, 3–14, https://doi.org/10.1175/WAF-832.1.

——, V. T. Wood, R. M. Steadham, R. R. Lee, B. A. Flickinger, and D. Sirmans, 2005b: New WSR-88D volume coverage pattern 12: Results of field tests. *Wea. Forecasting*, **20**, 385–393, https://doi.org/10.1175/WAF848.1.

Browning, K., 1964: Airflow and precipitation trajectories within severe local storms which travel to the right of the winds. *J. Atmos. Sci.*, **21**, 634–639, https://doi.org/10.1175/1520-0469(1964)021<0634:AAPTWS>2.0.CO;2.

Chrisman, J. N., 2011: Supplemental adaptive intra-volume low-level scan (SAILS). NWS Radar Operations Center Doc., 13 pp., http://www.roc.noaa.gov/wsr88d/PublicDocs/NewTechnology/SAILS_Initial_Presentation_Sep_2011.pdf.

——, 2014: Multiple elevation scan option for SAILS (MESO-SAILS). NWS Radar Operations Center Doc., 27 pp., http://www.roc.noaa.gov/wsr88d/PublicDocs/NewTechnology/MESO-SAILS_Description_Briefing_Jan_2014.pdf.

Doswell, C. A., III, and D. W. Burgess, 1993: Tornadoes and tornadic storms: A review of conceptual models. *The Tornado: Its Structure, Dynamics, Prediction, and Hazards*, *Geophys. Monogr.*, Vol. 79, Amer. Geophys. Union, 161–172.

Doviak, R. J., 2017: A memorandum on comparisons of weather and aircraft surveillance radar requirements to determine key features for a 10-cm MPAR and SENSR. NOAA/NSSL Rep., 41 pp.

——, and D. Zrnić, 1984: *Doppler Radar and Weather Observations.* Dover, 458 pp.

Klein, G., B. Moon, and R. R. Hoffman, 2006: Making sense of sensemaking 1: Alternative perspectives. *Intell. Syst.*, **21**, 70–73, https://doi.org/10.1109/MIS.2006.75.

Kumjian, M. R., 2013: Principles and applications of dual-polarization weather radar. Part I: Description of the polarimetric radar variables. *J. Oper. Meteor.*, **1**, 226–242, https://doi.org/10.15191/nwajom.2013.0119.

Lemon, L. R., 1998: The radar "three-body scatter spike": An operational large-hail signature. *Wea. Forecasting*, **13**, 327–340, https://doi.org/10.1175/1520-0434(1998)013<0327:TRTBSS>2.0.CO;2.

——, and C. A. Doswell III, 1979: Severe thunderstorm evolution and mesocyclone structure as related to tornadogenesis. *Mon. Wea. Rev.*, **107**, 1184–1197, https://doi.org/10.1175/1520-0493(1979)107<1184:STEAMS>2.0.CO;2.

Nai, F., J. Boettcher, C. Curtis, D. Schvartzman, and S. Torres, 2020: The impact of elevation sidelobe contamination on radar data quality for operational interpretation. *J. Appl. Meteor. Climatol.*, **59**, 707–724, https://doi.org/10.1175/JAMC-D-19-0092.1.

NOAA, 1991: WSR-88D program. NWS Radar Operations Center, https://www.roc.noaa.gov/WSR88D/WSR88DProgram.aspx.

Piltz, S. F., and D. W. Burgess, 2009: The impacts of thunderstorm geometry and WSR-88D beam characteristics on diagnosing supercell tornadoes. *34th Conf. on Radar Meteorology*, Williamsburg, VA, Amer. Meteor. Soc., P6.18, https://ams.confex.com/ams/34Radar/techprogram/paper_155944.htm.

Saxion, D. S., and R. L. Ice, 2012: New science for the WSR-88D: Status of the dual-polarization upgrade. *28th Conf. on Interactive Information Processing Systems*, New Orleans, LA, Amer. Meteor. Soc., https://ams.confex.com/ams/92Annual/webprogram/Paper197645.html.

Simmons, K. M., and D. Sutter, 2009: False alarms, tornado warnings, and tornado casualties. *Wea. Climate Soc.*, **1**, 38–53, https://doi.org/10.1175/2009WCAS1005.1.

Smith, B. T., R. L. Thompson, J. S. Grams, and J. C. Broyles, 2012: Convective modes for significant severe thunderstorms

in the contiguous United States. Part I: Storm classification and climatology. *Wea. Forecasting*, **27**, 1114–1135, https://doi.org/10.1175/WAF-D-11-00115.1.

Thompson, R., and Coauthors, 2017: Tornado damage rating probabilities derived from WSR-88D data. *Wea. Forecasting*, **32**, 1509–1528, https://doi.org/10.1175/WAF-D-17-0004.1.

Torres, S., and C. Curtis, 2007: Initial implementation of super-resolution data on the NEXRAD network. *23rd Int. Conf. on Interactive Information and Processing Systems for Meteorology, Oceanography, and Hydrology*, San Antonio, TX, Amer. Meteor. Soc., 5B.10., https://ams.confex.com/ams/87ANNUAL/techprogram/paper_116240.htm.

WDTD, 2021: Impact based warning guidance. Accessed 17 March 2021, https://training.weather.gov/wdtd/courses/woc/severe/storm-structures-hazards/tornado/twg3-now/presentation_content/external_files/30-40-50.png.